CLASSIFICATION:
Physical Sciences - Earth, Atmospheric, and Planetary Sciences

TITLE:
The First Day of the Cenozoic

Sean P. S. Gulick[1,2], Timothy Bralower[3], Jens Ormö[4], Brendon Hall[5], Kliti Grice[6], Bettina Schaefer[6], Shelby Lyons[3], Katherine H. Freeman[3], Joanna Morgan[7], Natalia Artemieva[8], Pim Kaskes[9], Sietze J. de Graaff[9], Michael Whalen[10], Gareth Collins[7], Sonia M. Tikoo[11], Christina Verhagen[11], Gail L. Christeson[1], Philippe Claeys[9], Marco Coolen[6], Steven Goderis[9], Kazuhisa Goto[12], Richard Grieve[13], Naoma McCall[1,2], Gordon Osinski[13], Auriol Rae[7], Ulrich Riller[14], Jan Smit[15], Vivi Vajda[16], Axel Wittmann[17], and the Expedition 364 Scientists

[1]Institute for Geophysics, Jackson School of Geosciences, University of Texas at Austin, USA 78758
[2]Department of Geological Sciences, Jackson School of Geosciences, University of Texas at Austin, USA 79712
[3]Department of Geosciences, Pennsylvania State University, University Park, USA 16801
[4]Centro de Astrobiología INTA-CSIC, Instituto Nacional de Técnica Aeroespacial, 28850 Torrejon de Ardoz, Spain
[5]Enthought, Inc., 200 W Cesar Chavez St Suite 202, Austin, TX USA 78701
[6]Western Australian Organic and Isotope Geochemistry Centre, The Institute for Geoscience Research, School of Earth and Planetary Science, Curtin University, Perth, WA, Australia 6102
[7]Department of Earth Science and Engineering, Imperial College London, UK SW7 2AZ
[8]Planetary Science Institute, Tucson, AZ USA 85719-2395
[9] Analytical, Environmental and Geo-Chemistry, Vrije Universiteit Brussel, Brussels, Belgium
[10]Department of Geosciences, University of Alaska Fairbanks, USA 99775
[11]Department of Earth and Planetary Sciences, Rutgers University, New Brunswick, New Jersey, USA 08854
[12]Tohoku University, International Research Institute of Disaster Science, Sendai, Japan
[13] Department of Earth Sciences, University of Western Ontario, Canada N6A 3K7
[14] Institut für Geologie, Universität Hamburg, Hamburg, Germany 20146
[15] Faculty of Sciences (FALW), Vrije Universiteit Amsterdam, Netherlands
[16] Swedish Museum of Natural History, Stockholm, Sweden
[17] Eyring Materials Center, Arizona State University, Tempe, USA 85287-1704

CORRESPONDING AUTHOR:
Sean P.S. Gulick, Institute for Geophysics, University of Texas at Austin, 10100 Burnet Rd Bldg ROC, Austin, Texas 78758; sean@ig.utexas.edu; 512-471-0483

KEYWORDS:
Chicxulub, Impact Crater, Melt, Suevite, Cretaceous-Paleogene, K-Pg, Mass Extinction, Peak Ring, Tsunami

Abstract

Highly expanded Cretaceous-Paleogene (K-Pg) boundary section from the Chicxulub peak ring, recovered by IODP-ICDP Expedition 364, provides an unprecedented window into the immediate aftermath of the impact. Site M0077 includes ~130-m of impact melt rock and suevite deposited the first day of the Cenozoic, covered by < 1m of micrite-rich carbonate deposited over the subsequent weeks to years. Here, we present an interpreted series of events based on analyses of these drill cores. Within minutes of the impact, centrally uplifted basement rock collapsed outwards to form a peak ring capped in melt rock. Within tens of minutes, the peak ring was covered in ~40 m of brecciated impact melt rock and coarse-grained suevite including clasts possibly generated by melt-water interactions during ocean resurge. Within an hour, resurge crested the peak ring depositing a 10 m-thick layer of suevite with increased particle roundness and sorting. Within hours, the full resurge deposit formed through settling and seiches resulting in an 80-m-thick fining-upwards, sorted suevite in the flooded crater. Within a day, the reflected rim-wave tsunami reached the crater depositing a cross-bedded sand-to-fine gravel layer enriched in polycyclic aromatic hydrocarbons overlain by charcoal fragments. Generation of a deep crater open to the ocean allowed rapid flooding and sediment accumulation rates among the highest known in the geologic record. The high-resolution section provides insight into the impact environmental effects including charcoal as evidence for impact-induced wildfires and a paucity of sulfur-rich evaporites from the target supporting rapid global cooling and darkness as extinction mechanisms.

Significance

Chicxulub impact crater cores from the peak ring include ~130-m of impact melt rock and breccia deposited on the first day of the Cenozoic. Within minutes of the impact, fluidized basement rocks formed a ring of hills which were rapidly covered by ~40-m of impact melt and breccia. Within an hour, ocean waters flooded the deep crater through a northeast embayment depositing a further 90 m of breccia. Within a day, a tsunami deposited material

from distant shorelines including charcoal. Charcoal and absence of sulfur-rich target rocks support the importance of impact-generated fires and release of sulfate aerosols for global cooling and darkness post-impact.

/body

Introduction

Impacts of asteroids and comets are a dominant geologic process on rocky planets (**1**). The largest impact structures- peak ring craters and multi-ring impact basins- exhibit annular rings of elevated topography surround their centers, called peak rings. In 2016 a peak ring was drilled for the first time at the ~200-km-diameter Chicxulub impact structure (Fig. 1) during International Ocean Discovery Program (IODP)-International Continental Scientific Drilling Program (ICDP) Expedition 364 (**2, 3**). Drill core showed that the bulk of the Chicxulub peak ring was formed from uplifted, fractured, and shocked granitic rocks with unusually low density and seismic velocity, cross-cut by magmatic sheet intrusions and shear zones (**2, 4**). These results support the dynamic collapse model for peak-ring formation (**5**), in which rocks temporarily flow like a viscous fluid, moving inwards and upwards to form a zone of central uplift, then collapse outwards and downwards to form a peak ring (e.g., **6**). Within tens of seconds of the impact a ~40-50-km radius transient cavity was formed (Fig. 2A, B) and lined with impact melt (**5)**. The main mass of this melt ends up inside the peak ring, forming the central impact melt sheet, (Fig. 2), but some melt drapes and covers the peak ring, and extends into the annular trough (**7-9**).

Impact cratering is an extremely energetic process that results in the formation of a variety of breccia layers within and outside craters. One of the characteristic impact breccias is a polymict melt-bearing breccia, informally termed suevite, that contains shocked clasts (e.g., **10-12**). Emplacement mechanisms for suevite vary among and within craters, and with marine and non-marine settings (**13-17, 18-20**). Additionally, the sources of the material in these impactites are debated (**21**). For instance, occurrences of suevite have been attributed to a melt-rich flow from the overshooting central uplift during crater collapse (**13**) or to melt-

57 water interaction similar to molten fuel coolant interaction (MFCI) in volcanic processes (**16,**
58 **22-24**).
59
60 The K-Pg impact event resulted in a globally distributed ejecta layer which, at distal sites (>
61 6000 km from Chicxulub), is highly condensed (2-3 mm thick) and contains altered
62 microkrystites and shocked minerals (e.g., **25**). These impact deposits, which formally were
63 deposited within the Cenozoic (Danian) (**26**), thicken and becomes more stratigraphically
64 complex with proximity to the crater (**25**). K-Pg boundary sections around coastal and shelf
65 sites in the Gulf of Mexico and Caribbean show a mixture of material delivered by airfall,
66 shelf collapse, debris flows, and tsunami (**27-32**). Within the deep-water Gulf of Mexico,
67 earthquake energy from the impact triggered gravity flows on continental slopes generating
68 the largest known event deposit on Earth (**33**). Within the Chicxulub impact structure, the
69 boundary event deposit was drilled onshore within the annular trough, (sites ICDP
70 Yaxcopoil-1 and Yucatan-6), and the central basin (sites Sacapuc-1 and Chicxulub-1) (Fig.
71 1) (**11, 34-36**).
72
73 These records of the K-Pg boundary offer critical insights into the environmental effects of
74 the Chicxulub impact and connections to the global extinction event (**25, 37**). The
75 sedimentary target rocks, comprised of volatile-rich, marine carbonates and evaporites, have
76 been a key focus of studies considering possible extinction mechanisms (**38-43**). Yaxcopoil-
77 1 penetrated an intact Cretaceous Albian to Campanian slump block that consisted of 27%
78 anhydrite and >70% carbonates (**44, 45**). Studies of the deposits outside the crater suggest
79 that the deeper sedimentary target may have been even more evaporite-rich (49-60%
80 anhydrite) (**46, 47**). In the atmosphere, sulfate combines with water vapor to form sulfate
81 aerosols that impede solar insolation; models of global climate response to a conservative
82 100 Gt of sulfur released by the Chicxulub impact into the K-Pg atmosphere indicated that
83 global surface temperatures would have declined by > 20°C and that disruption of the

Earth's climate could have lasted ~30 years (**48**). This scenario is consistent with proxy data indicating sea surface cooling in the months to years following the impact (**30**).

A sudden release of 425±60 Gt of CO_2 and 325±60 Gt of S was recently calculated by Artemieva et al. (**49**) using new constraints for the impact angle and direction of the Chicxulub impactor from Collins et al. (**50**); these larger sulfate amounts might result in prolonged cooling. Further, mössbauer analysis of boundary clay from proximal and distal sites have revealed that Fe nanoparticles, formed during the impact, served as nuclei for aerosols causing prolonged darkness (**51, 52**). Ejecta descending from high altitudes can radiate heat, and potentially ignite wildfires (**53-57**). Soot within the K-Pg boundary layer indicates that extensive impact-induced fires occurred instantaneously or within months of the impact (**58**), and could have intensified global cooling (**59**). One of the major objectives of drilling at the peak ring was to explore evidence for the drivers of these profound environmental changes that were potentially responsible for the severity of the mass extinction at the K-Pg boundary.

IODP-ICDP Expedition 364 drilled into the offshore portion of the Chicxulub impact crater (**2, 3**). Site M0077 (Fig.1) was located high on the topographic peak ring providing a unique setting for examining the K-Pg boundary within the crater; the site was selected based on seismic images that suggested that the K-Pg boundary was located in a valley within the peak ring which itself is elevated ~400 m above the crater floor. We proposed that this location would preserve the full sequence of impact-related rocks and transition into the earliest Paleogene without significant erosion from post-impact slumping induced by earthquake aftershocks (Figure 1). Site M0077 recovered core from 505.70-1334.73 mbsf (meters below seafloor) at nearly 100% recovery (**2, 3**).

Observations of the K-Pg Boundary Sedimentary Sequence

The recovered core at Site M0077 is broadly subdivided into four units (Figure 1) (**60**). Unit 1 is 111.63-m-thick post-impact sedimentary rock. Unit 2 is 104.28-m-thick and dominantly suevite. Unit 3 is 25.41-m-thick impact melt rock with some clasts present. Unit 4 consists of shocked granitic target rocks, pre-impact sheet intrusions and intercalations of suevite and impact melt rock. Here, we examine the sedimentology and geochemistry of Unit 1G, referred to as the Transitional Unit (**61**), and Units 2 and 3, which constitute the upper peak-ring impactites cored from 617.34 to 747.14 mbsf. Here we provide core descriptions, 0.3 mm resolution X-ray CT imaging of clasts, matrix and structure, paleomagnetic data, visual line logging of clasts within the cores ≥ 0.5 cm in size, and machine learning identification and analysis of clast size, shape, and sorting for the ~130 m thick K-Pg boundary deposit. Smear slide observations and organic geochemical analyses were made of samples in the uppermost ~3 meters of the section of Unit 2A and Unit 1G.

Photos of the split cores of Unit 3 (Fig. 1b) illuminate an upwards transition from impact melt rock (Unit 3) to breccia largely consisting of black impact melt rock fragments within a green and gray matrix (Unit 2C). The upper portions of Unit 3 and lower parts of Unit 2 also include large target rock clasts. Thus, we describe this section as including impact melt rock, impact melt rock breccia, and suevite (Fig. 1b). Within Unit 2, the overall clast size decreases upcore.

Geological line logging applied on Unit 2 (the suevite interval) was used to catalog all clasts larger than 5 mm along a transect of the cores from 672.01 - 715.93 mbsf (Fig. 3, see Methods). Analyzed parameters included clasts/meter, clast size, matrix versus clast supported grains, roundness, sorting, and a broad categorization of lithology. From 706.00-715.93 mbsf clasts per meter were low (<50), clast sizes were up to 10 cm, roundness increased from angular to sub-angular, and the section was poorly sorted (Fig. 3). Lithologically, the abundance of clasts in this lower section was >60% impact melt rock, ~20% sedimentary target rocks (carbonate, siltstone, and chert), and ~10% crystalline target

rocks. In contrast, from 698.00-706.00 mbsf clasts per meter increased by ~50%, clast size decreased, and roundness and sorting increased upcore (Fig. 3). The proportion of melt rock fragments increased by ~10% in this interval at the expense of carbonate target rock clasts. From 672.01-698.00 mbsf the number of clasts per meter and sorting increased and clast size decreased upsection. The abundance of crystalline target rock clasts in the clast population decreased to <5% in this interval and the abundance of sedimentary target clasts increased. None of the 2793 clasts examined by the geological line logging method were identified as evaporites (anhydrite, gypsum or halite).

Lithology and geochemistry of Unit 2, both matrix and clasts, were also examined using 50 2-cm-long samples (**60**). Each sample was classified by its mineral mode and chemical composition using bulk powder X-ray diffraction (XRD) analysis and X-ray fluorescence (XRF). The total percentage of gypsum and anhydrite recorded by XRD was 0.73% and 0.04%, respectively. Furthermore, no anhydrite or gypsum minerals were observed in petrographic examination of 85 thin sections and less than 0.7 wt% S was determined in micro-X-ray flourescence (μXRF) scans of 53 thin sections and LECO CS-300 carbon-sulfur analyses (see Methods (SI Appendix, Fig. S1, S2)) (**60**). There are three outliers, two of which (core 40R-1: 0.63 wt% and 40R-2: 0.44 wt% S) are identified as pyrite (FeS_2) grains by μXRF and petrographic observation (SI Appendix, Fig. S3). The third outlier detected by carbon-sulfur analysis (core 74R-1: 0.43 wt% S) is also likely pyrite. Lastly, detailed petrographic analyses of 12 suevite samples were performed using electron beam methods and no anhydrite or gypsum were observed (see Methods). In summary, our multi-method analysis determined that the suevite sequence in the IODP-ICDP 364-core was almost entirely devoid of gypsum and anhydrite, and sulfur-bearing phases were limited to pyrite, chalcopyrite, and minor accessory minerals (**3**).

In addition to line logging, a machine learning routine was developed to analyze clast characteristics using high-resolution core photographs (Fig 3, Methods). A convolutional

neural network extracted features based on textural patterns and then clasts were classified using a segmentation routine (SI Appendix, Fig. S4). Clast size, roundness and sorting, area per meter, and clast versus matrix support were determined from the data. These values are compared to the line logging analyses of the same characteristics on the transect of clasts (Fig. 3). Both methods showed that: (1) the numbers of clasts and clast size were inversely correlated; (2) within the analyzed breccia, a shift from clast to matrix supported occurred between 708 and 706 mbsf; (3) the interval from 698-706 mbsf represented a transition in roundness, sorting, and clast size; and (4) above ~690 mbsf numbers of clasts, matrix support, and sorting increased, while clast sizes decreased.

X-ray CT images of the 3D scans of the Site M0077 cores yielded information on the relative CT numbers (a proxy for density) of the matrix and clasts throughout the suevite (SI Appendix, Fig. S5). Key CT observations are that: (1) the black impact melt rocks (Fig. 1) in Unit 3B included partially digested clasts (SI Appendix, Fig. S5); (2) clasts of the black impact melt rock in Unit 3A were observed in a matrix of the green impact melt rock (Fig 1); (3) in Unit 2C the matrix transitioned from a higher CT number (light grey in SI Appendix, Fig. S5) characteristic of melt rock in Unit 3 to a lower CT number (darker grey in SI Appendix, Fig. S5) identified with the electron microprobe as a calcite, silica, and zeolite groundmass observed throughout the suevite in Units 2A and 2B; (4) from 698-706 mbsf in Unit 2B the matrix was relatively uniform and the interval included the shallowest multi-centimeter clasts; (5) in Units 2A and 2B above 698 mbsf fining upward clast sizes dominated, (6) in Unit 2A local reverse grading was observed and from 617.5-625 mbsf some layering is present (e.g., Fig 4C,H,I); and (7) the interval from 617.34-617.44 mbsf in Unit 2A was a 10 cm thick unidirectional cross-bedded deposit (Fig. 4F,G).

Point counting of recovered cores (see Methods; SI Appendix, Fig. S6) extended the sedimentological analyses of the clast sizes upcore from 672-617 mbsf (where line-logging left off); these data showed the general upward increase in sorting continued throughout the

193 remainder of Unit 2. The upper portion of the Unit 2A suevite (627-617.34 mbsf), where
194 layering was observed in CT data, consisted of ~25 normally graded beds (e.g., Fig. 4H,I; SI
195 Appendix, Fig. S5A) beneath the 10 cm-thick cross bedded interval (Fig. 4F,G). These
196 normally graded beds fined upward from pebble- or sand-sized to silt and clay-sized
197 material. Locally, clays and other insoluble materials were concentrated along stylolites at
198 the tops of the graded beds. The upper few centimeters of Unit 2A contain abundant
199 reworked Maastrichtian planktic foraminifera.
200
201 Paleomagnetic analyses were also used as a tool to infer depositional processes (see
202 Methods, SI Appendix, Fig. S7). At the time of the impact, during magnetic chron 29r, the
203 expected geomagnetic inclination at the location of Chicxulub crater was ~-46°. If impactites
204 were emplaced above the Curie temperature of magnetite (580° C) and cooled *in situ*, these
205 deposits would be expected to uniformly record a full thermal remanent magnetization with
206 inclination ~-46°. This expected result was the case for Units 3 and 2C. However, Units 2A
207 and 2B included samples with highly scattered (both positive and negative) magnetic
208 inclination values, suggesting that the constituents of these samples did not experience
209 sufficient heating to thermally reset their pre-depositional magnetization directions following
210 their emplacement.

211 Lying above the cross-bedded interval at the top of Unit 2 is the Transitional Unit (Unit 1G), a
212 75-cm thick micrite-rich limestone (Fig. 4C) that included the initial appearance of life at the
213 impact site (**61**). The lower 37 cm of Unit 1G is comprised of about 39 fining upward couplets
214 of lighter (coarser) and darker (finer) material that overall fined upward. Maximum grain size
215 in these couplets decreased from 5.6 mm in basal Unit 1G down to less than 0.3 mm in the
216 uppermost portion of the unit. Based on the grain sizes of these couplets (**62**), repetitive
217 currents with velocities up to 100 cm/s were indicated at the base of Unit 1G with reduced
218 velocities of less than 25 cm/s in the upper part.

Organic biomarker analyses conducted across the top of Unit 2A and within Unit 1G (Core 40) showed concentrations of polyaromatic hydrocarbons (PAHs) associated with the process of combustion (**63-65**) were present below the cross-bedded layer and then increased by 2-3 orders of magnitude into the overlying high-energy cross-bedded layer (Fig. 4D). The molecule perylene, indicative of terrestrial organic matter (**66**), is the dominant PAH in the high-energy layer. The abundance of PAHs then collectively decreased upwards into Unit 1G (Fig. 4D).

High-grade charcoal was observed in two 1-3 cm zones in Unit 1G based on SEM and smear slide analysis (Fig. 4A, B). Upcore the first zone was centered at ~671.26 mbsf just above the base of Unit 1G; the second layer was positioned at ~616.56 mbsf just above the top of Unit 1G with the additional presence of charcoal observed in the overlying Unit 1F from ~616.50-616.52 mbsf. Sporadic grains of charcoal were dispersed throughout Unit 1G and at the top of Unit 2A (Fig. 4E). Based on 100 fields of view at 1600x magnification a total of 2096 charcoal specimens were identified between 617.25 and 617.36 mbsf and 1018 charcoal specimens within the interval 616.55 to 616.60 mbsf (Fig. 4E). The mean grain sizes were 3.78 micron and 3.53 micron, respectively (see Methods, SI Appendix, Fig. S8).

Interpretation for Impact Processes

Hole M0077A preserves a record of the first materials deposited on the Chicxulub peak ring in the immediate aftermath of the K-Pg impact. The deposit includes ~130 m of impact melt rock, melt rock breccia, and suevite. Our multi-disciplinary analyses of this sequence provide insights into the dominant geologic processes and environmental effects of this impact. We interpret these data building on previous impact modeling studies as to the sequential impact processes that occurred 66.0 Ma beginning in the moments after impact and ending when the crater is fully formed, flooded, and seiches (standing waves) and tsunami (shallow water waves reflected back into the impact basin) have subsided (Fig. 2).

245 Excavation Stage: In the first moments of the impact, variably shocked sedimentary and
246 crystalline target rocks were excavated by ballistic ejection and/or transport within an impact
247 plume, consisting of vaporized material, melt, and solid particles (Fig. 2B) (**40**). The
248 sedimentary target rocks contained 30-50% evaporites (**44-47**) and yet <1% of these sulfur-
249 rich minerals were identified by petrographic and geochemical analyses of the Site M0077
250 impactites. Based on thermodynamic and experimental data that suggest carbonates degas
251 at 60 –100 GPa and anhydrite at 25 – 125 GPa (**68, 69**), and the assumption that degassing
252 increases linearly with increasing pressure, led Artemieva et al. (**49**) to estimate that 325±60
253 Gt of S and 425±60 Gt of CO_2 were released by the high-velocity impact. If this assumption
254 is correct, then significant amounts of both carbonate and evaporite should have remained
255 within the basin and occurred as clasts in the suevite. The absence of evaporites in Site
256 M0077 may imply that degassing is not linear and that the amount of sulfate aerosol
257 produced has been underestimated. An alternative explanation for this absence is that non-
258 porous evaporites that did not degas were preferentially fractured into larger clasts than the
259 porous carbonates, which is consistent with experimental data (**68, 69**), and thus that
260 evaporites were more likely to be incorporated within the low-velocity ejecta and deposited
261 outside of the peak ring. In either case, our observations support sulfate aerosol–induced
262 global cooling and reduction of photosynthesis as an important kill mechanism at the K-Pg
263 boundary (e.g., **40, 48, 55**).
264
265 Crater Modification Stage including Initial Resurge: We interpret the 40+ m thick impact melt
266 rock, melt rock breccia, and suevite of Units 3 and 2C (706-747 mbsf; Fig. 1, 2D) as being
267 deposited rapidly by outward flowing melt and density currents carrying clasts of impact melt
268 rock. This interpretation is consistent with the uniformly negative paleomagnetic inclinations
269 recording the K-Pg boundary magnetic field, which require that Units 3 and 2C were
270 emplaced quickly and maintained, at least for a short time, at temperatures above 580°C.
271 The CT and visually-detected presence of partially digested crystalline clasts within the
272 impact melt rock implies uplifted basement rocks were incorporated into the melt during its

emplacement on top of the peak ring. Within the suevite, angular clasts of non-vesicular black impact melt rock entrained in a highly altered, clay-mineral-bearing, green groundmass suggests a deposit that could be the result of melt water interactions (MWI) (**23, 24, 70**), a term that is used here in contrast to MFCI. MFCI requires water droplets to be injected into the melt (**70**) and thus we prefer a more general suggestion of MWI which we envision to occur during an initial incursion of seawater in advance of the full resurge and flooding of the crater. Given the geomorphology of the crater, MWI would have been most likely in the central basin in the northeast quadrant of the crater where seawater would flow across the pool of impact melt (Fig. 2D right side), and any melt present in the annular trough (e.g., Fig. 2D left side).

Post-impact Resurge, Settling, Seiches, and Tsunami: The 600-1000 m deep Chicxulub crater floor is connected with the open ocean to the North-Northeast (see arrow in Fig. 1 inset) via a gap in the rim with water depths reaching ~ 2 km (**33, 43**). A rim-wave tsunami, formed by the outward uplift of the transient crater rim and the subsequent deposition of proximal ejecta into the shallow seas surrounding the crater (see Fig. 5 in **71**), would propagate outwards in all directions across the Gulf, where central Mexico was the closest shallow water region and shoreline. The subsequent return flow of water, the “resurge” into the crater, is expected to be dominated by ingress from the North-Northeast rim gap. Once large volume resurge waves enter the impact basin, phreatomagmatic-style events (MWI) will gradually switch off and substantially reducing temperatures at the seafloor (Fig. 2E). Simplified 1D “dam break” modeling of the flooding of the crater up to the depth of the peak ring (see Methods and SI Appendix, Fig. S9) suggests that the timing of full resurge is 30-60 minutes post-impact for a water depth at the crater rim exceeding 1 km. Complete flooding of the crater likely took considerably longer. We interpret the increase in rounding and sorting in Unit 2B from 698-706 mbsf to signify the return of ocean water (Fig. 2E, 3) and the fining upwards deposit from 617-698 mbsf (Fig. 3) to represent the bulk of the resurge deposit which occurred in a progressively flooding crater (Fig. 2F).

Evidence for the arrival of the resurge to the peak ring being recorded in the deposit from 698-706 mbsf includes: 1) the presence of the shallowest multi-centimeter clasts at ~698 mbsf, 2) that this layer is reduced in sonic velocities suggesting a higher porosity-more rapidly deposited section, and 3) a relatively continuous reduction in grain size and increase in sorting upcore above 698 mbsf (Fig. 3). Size sorting of large clasts near the base of Unit 2B, due to the presence of water, could be the cause for the observed low-frequency reflector present below the low-velocity zone that marks the suevite interval in seismic data (Fig. 1A) (**4**). The observation of both positive and negative paleomagnetic inclinations within samples from Unit 2B (SI Appendix, Fig. S7) suggests that this unit was deposited at lower temperatures than Unit 2C, as would be expected in a now flooded crater. A combination of entrained clasts retaining their pre-depositional magnetization and new magnetization produced by the creation of secondary magnetic minerals in a long-lived, post-impact hydrothermal system (**3**) are likely responsible for the observed variations in remanent magnetism.

The flooded crater likely continued to be a high-energy environment due to large magnitude earthquake aftershocks and gravity flow processes from the collapsed central uplift and the rapidly formed inner rim (**33**,**34**). We interpret the erosional contact at 642.57 mbsf at the base of Unit 2A as resulting from a gravity flow, and the presence of 25 graded beds within 2A (Fig. 4I) as evidence of seiches within the crater possibly triggered by earthquake energy and slumping. Chicxulub created Mw10-11 earthquakes (**33**) and the seismic shaking has been shown to generate seiches ~2000 km away in local basins (**72**). However, the bulk of Unit 2A continues to show fining upwards clast sizes and increasing sorting reflective of a settling process in a flooded crater with these punctuated higher-energy events (Fig. 2F).

The top of the suevites of Unit 2A (617.34 mbsf) is marked by a <10 cm thick cross-bedded interval. These structures exhibit a unidirectional flow path of sand- to fine gravel-sized

particles (Fig. 4F, G). The presence of low concentration of PAHs below the cross-bedded unit is interpreted to be generated by either combusted marine biomass, or reworked Cretaceous or older hydrocarbons in the target rocks. However, the increase in concentration of PAHs, particularly the terrestrial compound perylene, that is observed to peak in the cross-bedded layer Fig. 4) requires that a source of terrestrial material entered the crater during deposition of the uppermost Unit 2A (Fig 4D). The abundant reworked Maastrichtian planktic foraminifera at the top of Unit 2A indicate redeposition of sediments that were unconsolidated at the time of the impact. We therefore suggest that the uppermost 10 cm, cross-bedded suevite represents the return of the outward-directed rim wave tsunami reflected back from Gulf of Mexico coastlines which carried terrestrial signatures and suspended unconsolidated marine sediments (illustrated in Fig. 2G). The transport path was potentially across the shelf separating the Mexican highlands ~800 km to the West-Southwest from the newly formed crater. Based on modeling, the arrival time of the rim-wave tsunami wavetrains on the far side of the Gulf of Mexico was 2-3 hours after the impact (**33**) and reflections across the shelfal depths from the west are also likely hours in duration. Thus, we suggest that this tsunami energy was reflected back into the impact basin within the first day of the Cenozoic and that these tsunami waters were turbid and capable of transporting soil biomarkers.

Deposition of Unit 1G likely took place in less than a few years after the impact (**61**). We interpret the normal graded couplets within the lower part of this unit to represent a significant reduction in wave energy compared to Unit 2A as sedimentary features, such as cross bedding, are rare and grain size is considerably reduced (Fig. 4C). The decrease in grain size and lower energy couplets in Unit 1G imply lower magnitude aftershocks and/or gravity flows occurred in the impact basin over longer timescales than the seiches observed in Unit 2A.

Evidence for Fire: High abundances of charcoal are present in Unit 1G 4 cm above the top of the presumed tsunami deposit (Fig. 4), and within a few cm of the top of Unit 1G. The relationship of the lower layer with the high-energy deposit suggests that these particles were either transported into the crater by reflected tsunami but settled more slowly than the remainder of the material due to density differences as energy subsided, or are derived via airfall. Charcoal likely originated from impact-related combustion of forested landscapes surrounding the Gulf of Mexico as the impact site was entirely marine. The shallower charcoal layer (Fig. 4E) may reflect airfall with mixing into the overlying Unit 1F by bioturbation or reworking. Wildfires can be spawned in two ways by a large impact: directly by the impact plume or by re-entering ejecta (**56**, **73**, **74**). For Chicxulub, the plume is considered to emit sufficient thermal radiation to ignite flora up to 1000-1500 km from the impact site (**73**). High-velocity ejecta re-entering the Earth's atmosphere emits thermal radiation that is sufficient to ignite dry plant matter and char living flora at sites within a few thousand km from the crater, and may directly ignite living flora at more distal locations where the thermal pulse is delivered to the Earth's surface over a longer time period (**74**). Strong atmospheric disturbances associated with the impact could have extinguished some of these fires and emplaced unburnt, partially burnt or fully burnt plant materials within the atmosphere (**73**, **75**). Thus, the lower charcoal layer observed at Site M0077 could stem from charred proximal flora from the central Mexican shorelines ~800 km away, ignited by the impact plume, and delivered back to the crater by tsunami or other mechanisms. The shallow water depths to the south and south west of Chicxulub mean that the rim wave tsunami could have reflected from the central Mexican highlands and reach Chicxulub within hours of the impact without transiting deep water. The upper layers of charcoal were delivered to the crater years after the event (near top of Unit 1G) (**61**), probably from atmospheric rainout of fire-generated particles from wildfires around the globe.

Broader Implications

In summary, the Expedition 364 core of the Chicxulub peak ring contains the most complete and expanded record of the immediate aftermath of the K-Pg mass extinction to date. Generation of a deep crater, with a large opening in the rim that allowed rapid flooding of the crater by seawater, produced accumulation rates among the highest known in the geologic record (130 m/day). Preservation of these extreme sediment accumulation rates within the impact basin allows us to resolve the geological processes that occurred over minutes to years after the impact event. In particular, the recovered sedimentary section lacks evaporites, supporting impact-generated sulfate aerosol production and extinction mechanisms including global cooling and limitations on photosynthesis. The presence of melt breccia and suevite in cores suggest potential melt-water interactions, and rounding and sorting provide evidence for ocean resurge. Finally, graded beds, a cross bedded layer with terrestrial signatures, and charcoal provide evidence for seiches within the crater, a reflected tsunami, and some proximal fire generation within the first day of the Cenozoic.

Methods

Forty-one thin sections of the suevite interval between core sections 40-2 and 87-2 were examined for the presence of gypsum ($CaSO_4 \cdot 2H_2O$), anhydrite ($CaSO_4$) and halite (NaCl) under a transmitted light microscope. Clasts identified as possible halite or sulfate phases are analyzed by small trace elemental maps on a Bruker M4 Tornado µXRF scanner following the methodology of de Winter et al. (**76**). Thin sections from Unit 1G were examined microscopically under plane and cross polarized light using standard petrographic techniques. Bedding, lamination, ichnofabric, and other sedimentary structures were identified. Grains, matrix material and diagenetic products were classified, their mineralogy evaluated, and maximum grain size was measured using the microscope's reticle.

High-resolution, semi-quantitative major and trace elemental maps of 53 polished thick sections between core sections 40-2 and 96-2 were produced by using the Bruker M4 Tornado µXRF scanner available at the Vrije Universiteit Brussel (**76**) (SI Appendix, Fig. S1).

412 The elemental mapping measurements were executed using a Rh source and two XFlash
413 430 Silicon Drift detectors under vacuum conditions (20 mbar), with short acquisition times
414 per spot size (1 ms per spot with a size of 25 μm) and maximized source energy settings
415 (600 μA, 50 kV). Bulk compositions of the thick sections were quantified by identifying the X-
416 ray peaks in a representative boundary spectrum within the high-resolution color map. Major
417 elements were expressed as oxides (Na_2O, MgO, Al_2O_3, SiO_2, K_2O, CaO, TiO_2, MnO,
418 Fe_2O_3), whereas trace elements in elemental configuration, as these are present at much
419 lower concentration levels (P, S, Cl, V, Cr, Ni, Cu, Zn, Rb, Sr, Zr, Ba). The limit of
420 quantification of elemental sulfur in the M4 Bruker Tornado μXRF is conservatively
421 estimated to be 0.1 wt% (SI Appendix, Fig. S2). This limit is based on the quantification of
422 μXRF maps of pellets prepared from carbonate reference materials NIST SRM 1d (National
423 Institute of Standards & Technology, USA) and BCS CRM 513 (Bureau of Analyzed
424 Samples Ltd., UK). The limit of detection of S with this technique is 0.033 wt%.
425
426 Back-scattered electron imaging, energy-dispersive spectrometry, and X-ray intensity
427 mapping were used to describe the petrography of 12 suevite samples from the upper peak
428 ring section between 620 and 708 mbsf. This work was done with a JEOL-JXA 8530F
429 electron microprobe at Arizona State University's Eyring Materials Center. For imaging and
430 EDS analyses, an accelerating voltage of 15 kV, a beam current of 15 nA and a focused
431 beam were used. The X-ray intensity maps used an accelerating voltage of 20 kV, a beam
432 current of 60 nA, a dwell time of 20 milliseconds, and a beam diameter of 20 μm. These
433 supplemental studies confirmed the absence of anhydrite or gypsum in the studied suevite.
434
435 The Chicxulub cores were scanned using a Toshiba Aquilion Prime Dual Energy Helical CT
436 scanner at Weatherford Laboratories in Houston. This produces a series of axial cross
437 section maps of attenuation coefficients at two energy levels (135 kV and 85 kV). Each
438 cross section represents 0.3 mm of core depth, and have a spatial resolution of 0.25 mm.
439 Processing of the raw CT was performed by Enthought Inc. (**77**). CT depth values (mCCSF-

A) are artificially lengthened relative to drillers depth (called mbsf) due to overlaps in cores not being accommodated. CT images map the attenuation of X-rays at a given location in the core, this is represented using grayscale images where darker grays are low attenuation and light gray is high attenuation (Fig. 4E,F; SI Appendix Fig. S5). X-ray attenuation is correlated to both the bulk density and average atomic number of a sample region. Dual energy CT scans provide a mechanism to separate these effects (**78**).

Line-logging of drill cores is useful in the analysis of relative changes through the infill of impact craters, including slump and resurge deposits due to a marine target environment. This technique has been successfully applied to the Lockne, Tvären and Chesapeake Bay impact structures (**18-19, 79**). In this method, every clast with a length axis larger than a certain cut-off size (here 5mm) that touches a line drawn along the core is assessed for size, roundness and lithology (Fig. 3). Instead of using actual drill core, for the first time, this technique was applied to high-resolution core photos with the use of the image analysis software jMicrovision (version 1.2.7). In the suevite (M0077 Unit 2), 2376 clasts were analyzed between depths 672.01mbsf and 715.93mbsf and an evaluation of the nature of their groundmass, whether matrix- or clast-supported, was done (i.e., if clasts were in contact or not with adjacent clasts). Roundness was estimated with the use of grain shape comparitor, i.e., a standard diagram with drawings of grain shapes. Here, a diagram with only four shapes (i.e., angular, sub-angular, sub-rounded, rounded) was decided to be the most convenient (cf., **80**). CT images aided the lithological determinations. The lithologies were (preliminarily) classified into 17 categories that include a) melt rocks of different colors and textures, b) upper target (sedimentary rock, mainly carbonates), and c) lower target (crystalline rock and quartzite). The granulometric data were treated statistically as variations per meter, which allowed plots of clast frequency per meter and size sorting. Owing to the large amount of data, clast vs. matrix support was plotted as a ratio per meter. Uncertainty in clast size is largest for the smallest analyzed clasts. We estimate at 15 pixels

per mm, a 5 mm grain could have an 8% error in the clast size value but that this uncertainty reduces greatly with increasing clast size.

In order to efficiently examine a larger number of clasts, a deep learning model was applied to the high-resolution core photographs (Fig. 3). The pipeline has two stages; classification (SI Appendix, Fig. S4) and segmentation/shape analysis. In the classification step, a machine learning model is used to assign a lithology label to every pixel in the core photographs. The digital core photographs are RGB images and have 3 features directly associated with each pixel location - the amount of red, green and blue light that comprise the color of the pixel. This is local information, and classifying a pixel based only on color features neglects the spatial and textural context of a pixel. The images are passed to a pre-trained convolutional neural network (VGG-16, **81**) and intermediate activations are extracted forming a hypercolumn of spatial convolutions that provide textural features useful for classification (**82**). Training data are created by manually labeling representative pixels that belong to each of the lithology types represented in the core images. The labeled pixels along with their associated hypercolumns are used to train a machine learning model (XGBoost, **83**) to predict a lithology label for every pixel in the core images. The initial classification results are spatially regulated using a fully connected conditional random field (**84**). Individual clasts are observed in the classified images by identifying contiguous regions of pixels with the same lithology label that exceed a size threshold. Each clast is analyzed in terms of shape (perimeter, area), position, orientation and aspect ratio using the image analysis package scikit- image (**85**). The circularity of each clast ($4*\pi*area/perimeter$) is used as a roundness metric. The ratio of clast area to matrix area was calculated as a proxy for clast/matrix support.

Sedimentologic analyses include visual observation of the split cores and point counting. Point counting to determine clast-matrix percentages was completed using JMicrovision on

494 linescan images. Each value represents 300 points counted on each core piece (SI
495 Appendix, Fig. S6).
496
497 During the Expedition 364 Onshore Science Party (OSP), 83 non-azimuthally-oriented
498 paleomagnetic cylinders were obtained from Units 2 and 3 (SI Appendix, Fig. S7). These
499 samples were stepwise demagnetized using alternating field (AF) demagnetization up to at
500 least 85 mT and measured using 2G Enterprises superconducting magnetometers at
501 Rutgers University or CEREGE (France) or an AGICO JR-5 spinner magnetometer at
502 CEREGE. Characteristic magnetization directions were obtained for the highest coercivity,
503 origin-trending magnetization component within each sample using principal component
504 analysis (**86**). Ferromagnetic mineralogy and Curie temperatures were determined via high-
505 temperature magnetic susceptibility measurements using an AGICO Kappabridge
506 susceptibility meter at CEREGE.
507
508 Charcoal was first identified in smear slides using a Zeiss Axioskop microscope under
509 brightfield light at 1600x magnification. This illumination allowed the characteristic wood
510 structure to be observed. The distribution and character of charcoal in samples was
511 determined in thin sections using Zeiss Axioimager petrographic microscopes using
512 brightfield illumination. Grains were also observed in a FEI Nova NanoSEM 630 FE
513 scanning electron microscope. The relative abundance of charcoal was determined from the
514 area of grains in 25 fields of view at 1600x magnification using the National Institute of
515 Health's ImageJ software (SI Appendix, Fig. S8).
516
517 The flooding rate of the Chicxulub crater at the approximate location of the Expedition 364
518 drill site on the peak ring was estimated assuming resurge was dominated by ingress of
519 water from the deep pre-impact basin to the north-northeast (SI Appendix, Fig. S9).
520 Analytical solutions to the one-dimensional dam break problem (**87**) for three different dam
521 heights (h_0=0.5, 1 and 2 km) were found assuming that water entered the crater on one side

through a deep channel in the rim, flowed across the crater and reflected off the inside of the crater rim on the opposite (south-southwest) side of the crater. The different dam heights represent alternative estimates of the depth of water at the onset of the resurge. The upper estimate (2 km) represents the estimated maximum depth of the pre-impact basin at the edge of the crater and is consistent with the numerical impact simulation shown in Figure 5 of Collins et al. (**71**). Flooding of the crater up to the depth of the peak ring (500 m above the crater floor) is expected to take 30 minutes to one hour (SI Appendix, Fig. S9). The approximation neglects various factors that might delay the resurge, such as drag between the water and the crater floor and interactions between the flood water and the hot melt sheet, which might vaporize some of the water and generate MWI products.

In order to analyze the cores for biomarkers (Fig. 4D; SI Appendix Fig. S10), core samples (ca. 20 g) were surface cleaned by sonication in ultra-pure water two times for 15 min to remove any drilling fluid. After, the samples were freeze dried and three times sonicated for 15 min in dichloromethane and methanol (9:1 vol./vol.). After drying the samples were ground using a pestle and mortar and Soxhlet extracted for 72 hours using a mixture of dichloromethane and methanol (9:1 vol./vol.). The extracts were passed through a Pasteur pipette containing activated copper powder to remove the elemental sulfur. Excess solvent was carefully removed under nitrogen. The weighed extracts were then fractionated by small-scale column liquid chromatography. The sample (up to 10 mg) was applied to the top of a small column (5 × 0.5 cm i.d.) of activated silica gel (150 °C, 8 h). The saturated hydrocarbon fraction was eluted with n-hexane (4 mL), the aromatic hydrocarbon fraction with n-hexane and dichloromethane (4 mL, 9:1 vol./vol.), and the polar fraction with a mixture of dichloromethane and methanol (4 mL, 1:1 vol./vol.). The saturated and aromatic hydrocarbon fractions were analyzed by Gas Chromatography–Mass Spectrometry (GC–MS). GC–MS analysis was performed using an Agilent 5975B MSD interfaced to Agilent 6890 gas chromatograph, which was fitted with a DB-5MS UI capillary column (J and W Scientific, 60 m, 0.25 mm inner diameter, 0.25 μm phase thickness). The GC oven was

ramped from 40 to 325 °C at a heating rate of 3 °C/min with initial and final hold times of 1 and 30 min, respectively. Samples were dissolved in n-hexane and injected on-column using an Agilent 7683B auto-sampler. Helium (constant flow 27 cm/s) was used as the carrier gas. The MS was operating with ionization energy of 70 eV, a source temperature of 230 °C and an electron multiplier voltage of 1706 V, scanning a mass range of 50–550 amu. Aromatic hydrocarbon compounds were identified by comparison of mass spectra and by matching retention times with those of reference compounds reported previously (**88**). The unsubstituted PAHs including benzo(a)pyrene and perylene (ratio of these two PAHs shown in SI Appendix, Fig. S10) have a molecular ion of *m/z* 252. They were identified by comparing their retention times with those of reference compounds.

Acknowledgements

We thank captain and crew, drilling team, and technical staff who participated in shipboard and/or shore-based operations. The European Consortium for Ocean Research Drilling (ECORD) implemented Expedition 364 with funding from the International Ocean Discovery Program (IODP) and the International Continental scientific Drilling Project (ICDP). We thank the editor and two anonymous reviewers. Data and samples can be requested from IODP. U.S. participants were supported by the U.S. Science Support Program and NSF grants OCE 1737351, OCE 1736826, OCE 1737087, OCE 1737037, OCE 1736951, and OCE 1737199. J.V.M. was funded by NERC, Grant: NE/P005217/1. KG thanks ARC for grant number DP180100982 and ANZIC for funding. BS thanks Curtin University for an Australian Postgraduate Award. The VUB group is supported by Research Foundation Flanders (FWO), and BELSPO; Kaskes is a FWO PhD fellow. W. Zylberman and J. Gattacceca are thanked for assistance with paleomagnetic measurements. J. Ormö was partially supported by grants ESP2015-65712-C5-1-R, and ESP2017-87676-C5-1-R from the Spanish Ministry of Economy and competitiveness and Fondo Europeo de Desarrollo Regional. University of Texas Institute for Geophysics Contribution #3634.

References

1. Melosh, HJ (1989) *Impact cratering: a geologic process* (Oxford University Press, Oxford), Oxford Monographs on Geology and Geophysics, 11, 253 p.

2. Morgan, JV, et al. (2016) The formation of peak rings in large impact craters. *Science* 354(6314): 878-882.

3. Morgan, J, Gulick, S, Mellett, CL, Green, SL, and the Expedition 364 Scientists (2017) *Chicxulub: Drilling the K-Pg Impact Crater* (International Ocean Discovery Program), Proceedings of the International Ocean Discovery Program, 364, https://doi.org/10.14379/iodp.proc.364.2017

4. Christeson, G. L., et al. (2018), Extraordinary rocks from the peak ring of the Chicxulub impact crater: P-wave velocity, density, and porosity measurements from IODP/ICDP Expedition 364, *Earth Planet Sci Lett 495*: 1-11, doi:10.1016/j.epsl.2018.05.013.

5. Collins, GS, Melosh, HJ, Morgan, JV, Warner, MR (2002) Hydrocode simulations of Chicxulub crater collapse and peak-ring formation. *Icarus* 157(1): 24-33.

6. Riller, U, et al (2018) Rock fluidization during peak-ring formation of large impact structures. *Nature* 562(7728): 511-518.

7. Barton, PJ, et al (2010) Seismic images of Chicxulub impact melt sheet and comparison with the Sudbury structure. *Large meteorite impacts and planetary evolution IV*: 103-113.

8. Morgan, JV, et al (2011) Full waveform tomographic images of the peak ring at the Chicxulub impact crater. *J Geophys Res: Solid Earth* 116(B6), https://doi.org/10.1029/2010JB008015.

9. Gulick, SPS, et al (2013) Geophysical characterization of the Chicxulub impact crater. *Rev Geophys* 51(1): 31-52.

10. Shoemaker, EM, Chao, EC (1961) New evidence for the impact origin of the Ries Basin, Bavaria, Germany. *J Geophysl Res* 66(10): 3371-3378.

11. Claeys, P, Heuschkel, S, Lounejeva-Baturina, E, Sanchez-Rubio, G, Stöffler, D (2003) The suevite of drill hole Yucatán 6 in the Chicxulub impact crater. *Meteoritics & Planet Sci* 38(9): 1299-1317.

12. Stöffler, D, Grieve, R (2007) In *Metamorphic rocks: A classification and glossary of terms, recommendations of the International Union of Geological Sciences*, ed Fettes D, Desmons J, (Cambridge University Press, Cambridge), pp. 82–92, 111–125.

13. Osinski, GR, Grieve, RA, Spray, JG (2004) The nature of the groundmass of surficial suevite from the Ries impact structure, Germany, and constraints on its origin. *Meteoritics & Planet Sci* 39(10): 1655-1683.

14. Meyer, C, Jébrak, M, Stöffler, D, Riller, U (2011) Lateral transport of suevite inferred from 3D shape-fabric analysis: Evidence from the Ries impact crater, Germany. *GSA Bulletin* 123(11-12): 2312-2319.

15. Kring, DA (2005) Hypervelocity collisions into continental crust composed of sediments and an underlying crystalline basement: comparing the Ries (~ 24 km) and Chicxulub (~ 180 km) impact craters. *Chemie der Erde-Geochem* 65(1): 1-46.

16. Artemieva, NA, Wünnemann, K, Krien, F, Reimold, WU, Stöffler, D (2013) Ries crater and suevite revisited—Observations and modeling Part II: Modeling. *Meteoritics & Planet Sci* 48(4): 590-627.

17. Stöffler, D, et al (2013) Ries crater and suevite revisited—Observations and modeling Part I: Observations. *Meteoritics & Planet Sci* 48(4): 515-589.

18. Ormö, J, Sturkell, E, Lindström, M (2007) Sedimentological analysis of resurge deposits at the Lockne and Tvären craters: Clues to flow dynamics. *Meteoritics & Planet Sci* 42(11): 1929-1943.

19. Ormö, J, Sturkell, E, Horton Jr, JW, Powars, DS, Edwards, LE (2009) Comparison of clast frequency and size in the resurge deposits at the Chesapeake Bay impact structure (Eyreville A and Langley cores): clues to the resurge process. *Special Paper of the Geological Society of America* 458: 617-632.

20. Horton, JW, Gohn, GS, Powars, DS, Edwards, LE, Evans, K, King, DT, Morrow, JR (2008) Origin and emplacement of impactites in the Chesapeake Bay impact structure, Virginia, USA. *Special Paper of the Geological Society of America* 437: 73-97.

21. Osinski, GR, Grieve, RA, Chanou, A, Sapers, HM (2016) The “suevite” conundrum, part 1: The Ries suevite and Sudbury Onaping Formation compared. *Meteoritics & Planet Sci* 51(12): 2316-2333.

22. Wohletz, K, Heiken, G (1992) *Volcanology and geothermal energy* (University of California press, Berkeley), v 432.

23. Grieve, RA, Ames, DE, Morgan, JV, Artemieva, N (2010) The evolution of the Onaping Formation at the Sudbury impact structure. *Meteoritics & Planet Sci* 45(5): 759-782, doi: 10.1111/j.1945-5100.2010.01057.x

24. Wittmann, A, Kenkmann, T, Hecht, L, Stöffler, D (2007) Reconstruction of the Chicxulub ejecta plume from its deposits in drill core Yaxcopoil-1. *GSA Bulletin* 119(9-10): 1151-1167, doi: 10.1130/B26116.1

25. Schulte, P, et al (2010) The Chicxulub asteroid impact and mass extinction at the Cretaceous-Paleogene boundary. *Science* 327(5970): 1214-1218.

26. Gradstein, F. M. *Geologic Time Scale 2012, edited by J G Ogg, et al., Elsevier, 2012.*

27. Smit, J (1999) The global stratigraphy of the Cretaceous-Tertiary boundary impact ejecta. *Ann Rev Earth & Planet Sci* 27(1): 75-113.

28. Bourgeois, J, Hansen, TA, Wiberg, PL, Kauffman, EG (1988) A tsunami deposit at the Cretaceous-Tertiary boundary in Texas. *Science* 241(4865): 567-570.

29. Schulte, P, Smit, J, Deutsch, A, Salge, T, Friese, A, Beichel, K (2012) Tsunami backwash deposits with Chicxulub impact ejecta and dinosaur remains from the Cretaceous–Palaeogene boundary in the La Popa Basin, Mexico. *Sedimentology* 59(3): 737-765.

30. Vellekoop, J, et al (2014) Rapid short-term cooling following the Chicxulub impact at the Cretaceous-Paleogene boundary, *Proc Nat Acad Sci USA* 111: 7537-7541, doi: www.pnas.org/cgi/doi/10.1073/pnas.1319253111

31. Denne, RA, et al (2013) Massive Cretaceous-Paleogene boundary deposit, deep-water Gulf of Mexico: New evidence for widespread Chicxulub-induced slope failure. *Geology* 41(9): 983-986.

32. Renne, PR, et al (2018). Multi-proxy record of the Chicxulub impact at the Cretaceous-Paleogene boundary from Gorgonilla Island, Colombia. *Geology* 46(6):547-550, doi: https://doi.org/10.1130/G40224.1

33. Sanford, JC, Snedden, JW, Gulick, SP (2016) The Cretaceous-Paleogene boundary deposit in the Gulf of Mexico: Large-scale oceanic basin response to the Chicxulub impact. *J of Geophys Res: Solid Earth* 121(3): 1240-1261.

34. Hildebrand, AR, et al (1991) Chicxulub crater: a possible Cretaceous/Tertiary boundary impact crater on the Yucatan Peninsula, Mexico. *Geology* 19(9): 867-871.

35. Kring, DA, Boynton, WV (1992) Petrogenesis of an augite-bearing melt rock in the Chicxulub structure and its relationship to K/T impact spherules in Haiti. *Nature* 358(6382): 141-144.

36. Urrutia-Fucugauchi, J, Morgan, J, Stöffler, D, Claeys, P (2004) The Chicxulub scientific drilling project (CSDP). *Meteoritics & Planet Sci* 39(6): 787-790.

37. Alvarez, LW, Alvarez, W, Asaro, F, Michel, HV (1980) Extraterrestrial cause for the Cretaceous-Tertiary extinction. *Science* 208(4448): 1095-1108.

38. Brett, R (1992) The Cretaceous-Tertiary extinction: A lethal mechanism involving anhydrite target rocks. *Geochim et Cosmochim Acta* 56(9): 3603-3606.

39. Sigurdsson, H, D'Hondt, S, Carey, S (1992) The impact of the Cretaceous/Tertiary bolide on evaporite terrane and generation of major sulfuric acid aerosol. *Earth & Planet Sci Lett* 109(3-4): 543-559.

40. Pierazzo, E, Kring, DA, Melosh, HJ (1998) Hydrocode simulation of the Chicxulub impact event and the production of climatically active gases. *J Geophys Res: Planets* 103(E12): 28607-28625.

41. Bell, C, Morgan, JV, Hampson, GJ, Trudgill, B (2004) Stratigraphic and sedimentological observations from seismic data across the Chicxulub impact basin. *Meteoritics & Planet Sci* 39(7): 1089-1098.

42. Kring, DA (2007) The Chicxulub impact event and its environmental consequences at the Cretaceous–Tertiary boundary. *Palaeogeo Palaeoclim Palaeoeco* 255(1-2): 4-21.

43. Gulick, SP, et al (2008) Importance of pre-impact crustal structure for the asymmetry of the Chicxulub impact crater. *Nature Geosci* 1(2): 131-135.

44. Kenkmann, T, Wittmann, A, Scherler, D (2004) Structure and impact indicators of the Cretaceous sequence of the ICDP drill core Yaxcopoil-1, Chicxulub impact crater, Mexico. *Meteoritics & Planet Sci* 39(7): 1069-1088.

738 **45.** Belza, J, Goderis, S, Keppens, E, Vanhaecke, F, Claeys, P (2012) An emplacement
739 mechanism for the mega-block zone within the Chicxulub crater, Yucatán, Mexico based on
740 chemostratigraphy. *Meteoritics & Planet Sci* 47(3): 400-413.
741
742 **46.** Ramos, EL (1975) Geological summary of the Yucatan Peninsula. In *The Gulf of Mexico*
743 *and the Caribbean* (Springer, Boston), pp. 257-282.
744
745 **47.** Rebolledo-Vieyra, M, Urrutia-Fucugauchi, J (2006) Magnetostratigraphy of the
746 Cretaceous/Tertiary boundary and early Paleocene sedimentary sequence from the
747 Chicxulub Impact Crater. *Earth planets & space* 58(10): 1309-1314.
748
749 **48.** Brugger, J, Feulner, G, Petri, S (2017) Baby, it's cold outside: Climate model simulations
750 of the effects of the asteroid impact at the end of the Cretaceous. *Geophys Res Lett* 44(1):
751 419-427.
752
753 **49.** Artemieva, N, Morgan, J, Exp 364 Sci Party (2017) Quantifying the Release of Climate-
754 Active Gases by Large Meteorite Impacts With a Case Study of Chicxulub. *Geophys Res*
755 *Lett* 44(20): 10-180.
756
757 **50.** Collins, GS, et al (2017) Numerical simulations of Chicxulub crater formation by oblique
758 impact [presented at the 48th Lunar and Planetary Science Conference, The Woodlands,
759 Texas, 20–24 March 2017]. (Abstract 1832) https://www.hou.usra.edu/meetings/lpsc2017/
760 pdf/1832.pdf
761
762 **51.** Ferrow, E, Vajda, V, Bender-Koch, K, Peucker-Ehrenbrink, B, Willumsen, P (2011)
763 Multiproxy analysis of a new terrestrial and a marine Cretaceous-Paleogene (K-Pg)
764 boundary site from New Zealand. *Geochim et Cosmochim Acta* 75*(2*): 657-672.
765
766 **52.** Vajda, V, Ocampo, A, Ferrow, E, Bender-Koch, C (2015) Nano particles as the primary
767 cause for long-term sunlight suppression at high southern latitudes following the Chicxulub
768 impact –evidence from ejecta deposits in Belize and Mexico. *Gond Research* 27: 1079–1088,
769 doi:10.1016/j.gr.2014.05.009
770
771 **53.** Wolbach, WS, Lewis, RS, Anders, E (1985) Cretaceous extinctions: evidence for
772 wildfires and search for meteoritic material. *Science* 230(4722): 167-170.
773
774 **54.** Melosh, HJ, Schneider, NM, Zahnle, KJ, Latham, D (1990) Ignition of global wildfires at
775 the Cretaceous/Tertiary boundary. *Nature* 343(6255): 251-254.
776
777 **55.** Toon, OB, Zahnle, K, Morrison, D, Turco, RP, Covey, C (1997) Environmental
778 perturbations caused by the impacts of asteroids and comets. *Rev Geophys* 35(1): 41-78.
779
780 **56.** Kring, DA, Durda, DD (2002) Trajectories and distribution of material ejected from the
781 Chicxulub impact crater: Implications for postimpact wildfires. *J Geophys Res:*
782 *Planets* 107(E8): 6-22.
783
784 **57.** Durda, DD, Kring, DA (2004) Ignition threshold for impact-generated fires. *J Geophys*
785 *Res: Planets 109*(E8), doi:10.1029/2004JE002279
786
787 **58.** Morgan, J, Artemieva, N, Goldin, T (2013) Revisiting wildfires at the K-Pg boundary. *J of*
788 *Geophys Res: Biogeosciences* 118(4): 1508-1520.
789

790 **59.** Bardeen, CG, Garcia, RR, Toon, OB, Conley, AJ (2017) On transient climate change at
791 the Cretaceous− Paleogene boundary due to atmospheric soot injections. *Proc Nat Acad Sci*
792 *USA* 114(36): E7415-E7424.
793
794 **60.** Gulick et al (2017) Expedition 364 methods. *In* Morgan, J, Gulick, S, Mellett, CL, Green,
795 SL, Exp 364 Sci, *Chicxulub: Drilling the K-Pg Impact Crater.* Proceedings of the International
796 Ocean Discovery Program, 364 (International Ocean Discovery Program, College Station),
797 https://doi.org/10.14379/iodp.proc.364.102.2017
798
799 **61.** Lowery, CM, et al (2018) Rapid recovery of life at ground zero of the end-Cretaceous
800 mass extinction. *Nature* 558: 288-291.
801
802 **62.** Hjulstrom, J (1955) Transportation of detritus by moving water, In Trask, P.D., ed.,
803 Recent Marine Sediments, *SEPM Special Publication* 4, Doi:
804 https://doi.org/10.2110/pec.55.04.0005
805
806
807 **63.** Marynowski, L, Simoneit, BR (2009) Widespread Upper Triassic to Lower Jurassic
808 wildfire records from Poland: evidence from charcoal and pyrolytic polycyclic aromatic
809 hydrocarbons. *Palaios* 24(12): 785-798.
810
811 **64.** Denis, EH, et al (2012) Polycyclic aromatic hydrocarbons (PAHs) in lake sediments
812 record historic fire events: validation using HPLC-fluorescence detection. *Org geochem* 45:
813 7-17.
814
815 **65.** Karp, AT, Behrensmeyer, AK, Freeman, KH (2018) Grassland fire ecology has roots in
816 the late Miocene. *Proc Nat Acad Sci USA* 115(48):12130-12135, doi:
817 10.1073/pnas.1809758115
818
819 **66.** Grice, K, et al (2009) New insights into the origin of perlyene in geological samples.
820 *Geochimi et Cosmochim Acta* 73: 6531-6543.
821
822 **67.** Kowitz, A, et al (2016) Revision and recalibration of existing shock classifications for
823 quartzose rocks using low-shock pressure (2.5–20 GPa) recovery experiments and
824 mesoscale numerical modeling, *Meteoritics & Planet Sci* 51: 1741–176, doi:
825 10.1111/maps.12712
826
827 **68.** Gupta, SC, Ahrens, TJ, Yang, W (2001) Shock-induced vaporization of anhydrite and
828 global cooling from the K/T impact. *Earth Planet Sci Lett* 188(3-4): 399-412.
829
830 **69.** Prescher, C, Langenhorst, F, Hornemann, U, Deutsch, A (2011) Shock experiments on
831 anhydrite and new constraints on the impact-induced SOx release at the K-Pg
832 boundary. *Meteoritics & Planet Sci* 46(11): 1619-1629.
833
834 **70.** Liu, EJ, Cashman, KV, Rust, AC, Gislason, SR (2015) The role of bubbles in generating
835 fine ash during hydromagmatic eruptions. *Geology* 43: 239-242.
836
837 **71.** Collins, GS, et al (2008) Dynamic modeling suggests terrace zone asymmetry in the
838 Chicxulub crater is caused by target heterogeneity. *Earth & Planet Sci Lett* 270(3): 221-230.
839
840 **72.** DePalma, RA, et al (2019) A seismically induced onshore surge deposit at the KPg
841 boundary, North Dakota. *Proceeding Nat Acad (USA)* 116: 8190-8199.
842

73. Shuvalov, VV, Artemieva, NA (2002) Atmospheric erosion and radiation impulse induced by impacts, In Koeberl, C, MacLeod, KG, ed, *Catastrophic events and mass extinctions: Impacts and beyond: Geological Society of America Special Paper 356*: p. 695-703.

74. Belcher, CM, et al (2015) An experimental assessment of the ignition of forest fuels by the thermal pulse generated by the Cretaceous–Palaeogene impact at Chicxulub. *J Geol Soc* 172(2): 175-185.

75. Morgan, J., Artemieva, N., Goldin, T. (2013) Revisiting wildfires at the K-Pg boundary. *J Geophys Res* 118: 1508-1520.

76. de Winter, NJ, Claeys, P (2017) Micro X-ray fluorescence (μ XRF) line scanning on Cretaceous rudist bivalves: A new method for reproducible trace element profiles in bivalve calcite. *Sedimentology* 64(1): 231-251.

77. Hall, B, et al (2017) Dual energy CT-scanning and processing of core from the peak ring of the Chicxulub impact structure: results from IODP-ICDP Expedition 364, In *Lunar and Planetary Science Conference* 48: 1964.

78. Siddiqui, S, Khamees, AA (2004) Dual energy CT-scanning applications in rock characterization, SPE ATCE, SPE-90520, doi:10.2118/90520-MS

79. Sturkell, E, Ormö, J, Lepinette, A (2013) Early modification stage (preresurge) sediment mobilization in the Lockne concentric, marine-target crater, Sweden. *Meteoritics & Planet Sci* 48(3): 321-338.

80. Mazzullo, J, Graham, AG, Braunstein, C (1988). *Handbook for shipboard sedimentologists* (Ocean Drilling Program, College Station).

81. Simonyan, K, Zisserman, A (2015) Very deep convolutional networks for large-scale image recognition, arXiv:1409.1556

82. Hariharan, B, Arbelaez, P, Girshick, R, Malik, J (2015) Hypercolumns for object segmentation and fine-grained localization, *CVPR 2015*, arXiv:1411.5752v2

83. Chen, T, Guestrin, C (2016) XGBoost: A Scalable Tree Boosting System, *Proceedings of the 22nd ACM SIGKDD International Conference on Knowledge Discovery and Data Mining*, p. 785-794

84. Krähenbühl, P, Koltun, V (2011) Efficient Inference in Fully Connected CRFs with Gaussian Edge Potentials, *Adv Neural Info Proc Sys* 24: 109-117.

85. van der Walt, S, et al (2014) scikit-image: Image processing in Python. PeerJ 2:e453 doi:10.7717/peerj.453

86. Kirschvink, JL (1980). The least-squares line and plane and the analysis of palaeomagnetic data. *Geophys J Royal Astro Soc* 62(3), 699-718.

87. Stoker, JJ (1957). Water Waves. The Mathematical Theory with Applications. New York: Interscience Publ.

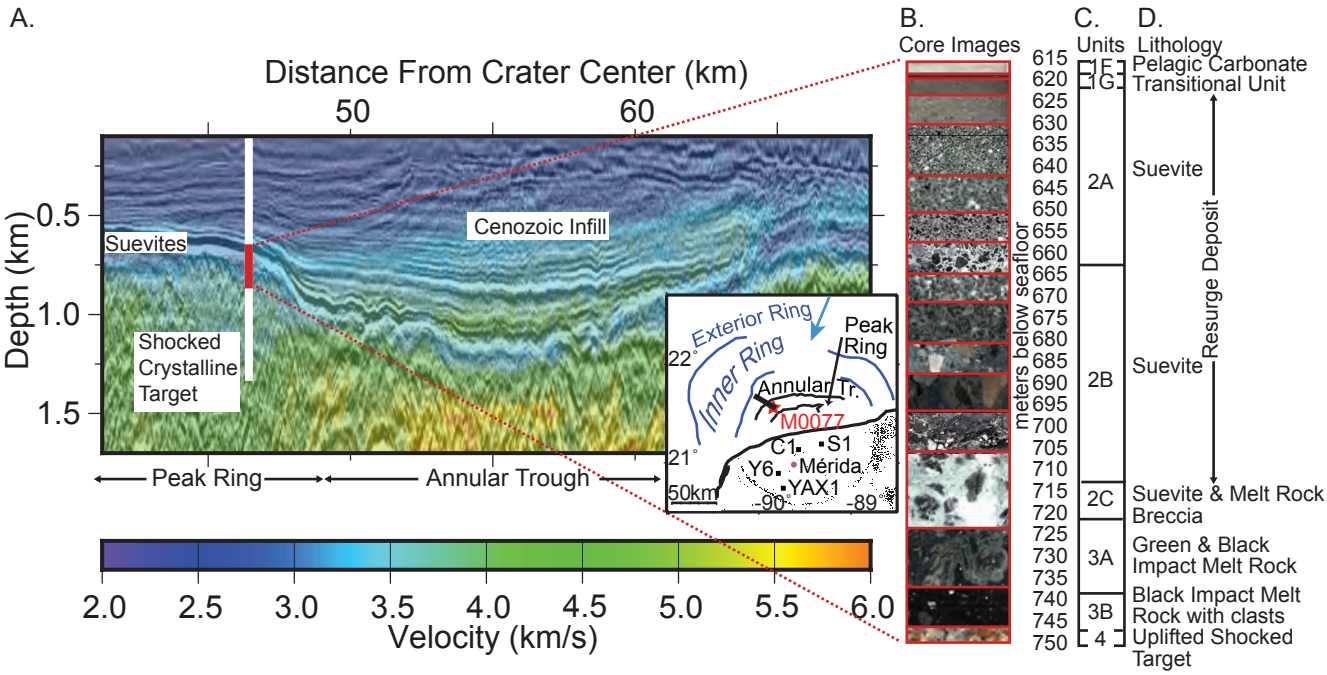
88. Grice, K, Nabbefeld, B, Maslen, E (2007) Source and Significance of Selected Polycyclic Aromatic Hydrocarbons in Sediments (Hovea-3 well, Perth Basin, Western Australia) Spanning the Permian-Triassic Boundary. *Org Geochem* 38: 1795-1803.

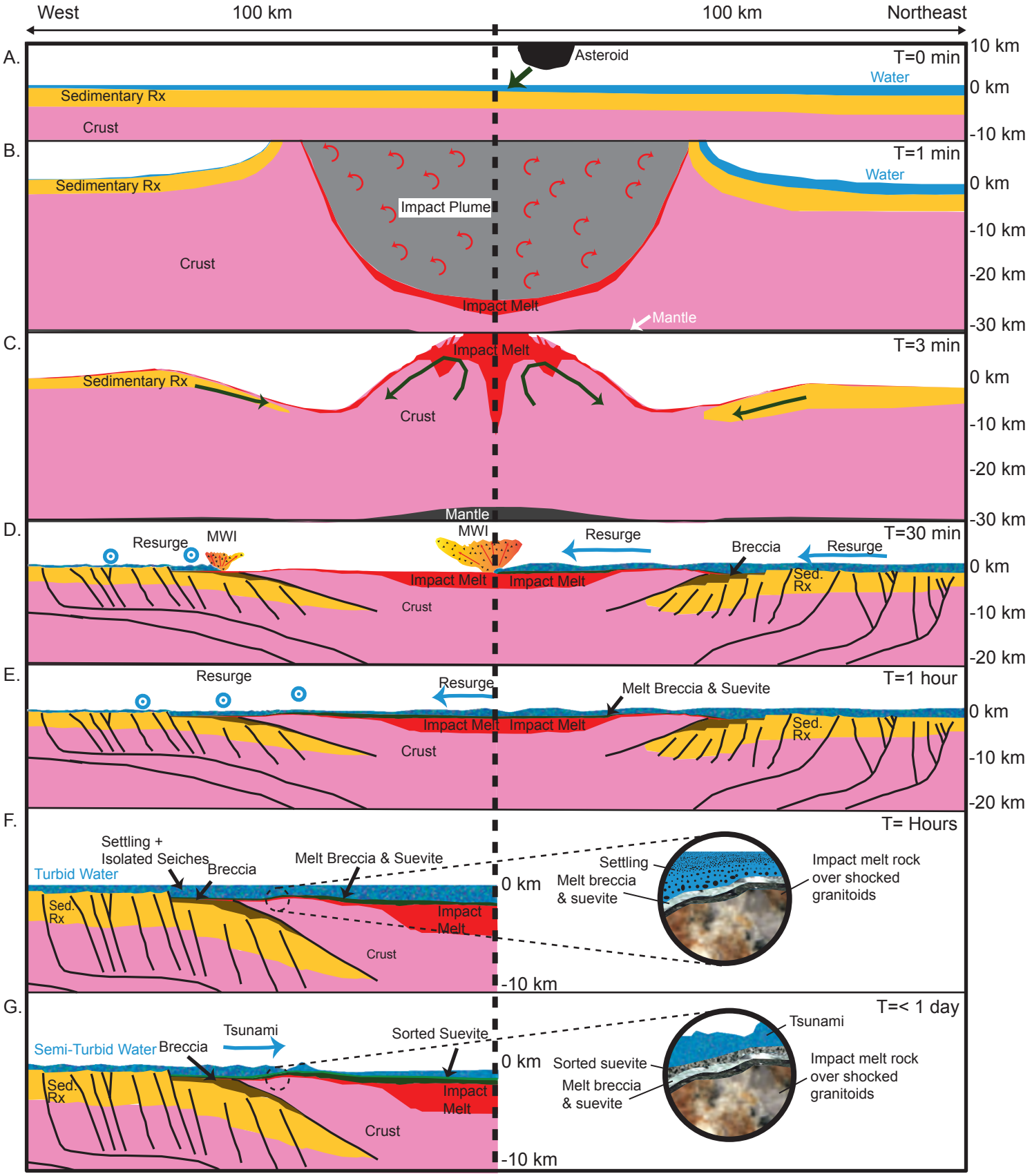
Figure Captions

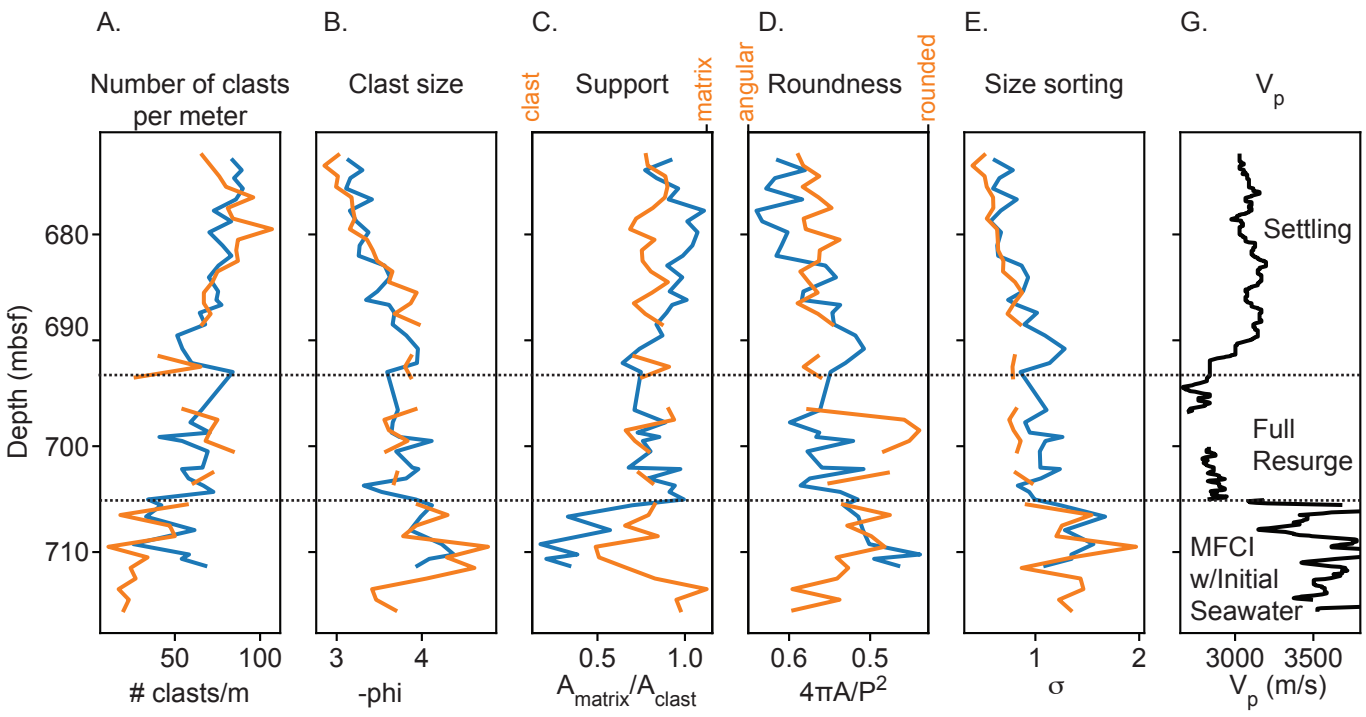
Figure 1. A. Seismic reflection image shown in depth with full waveform velocities overlain; line runs from southeast to northwest including the location of Site M0077 and radially outwards across the annular trough. The suevite interval within M0077, the focus of this paper, is shown in red which maps to a low-velocity zone beneath the crater floor. Inset map shows the location of crater rings, drill sites (see text), the seismic image, and direction that ocean waters re-entered the crater after formation. Expansion shows (B.) representative core images in stratigraphic order with depths, (C.) lithologic units, and (D.) lithology.

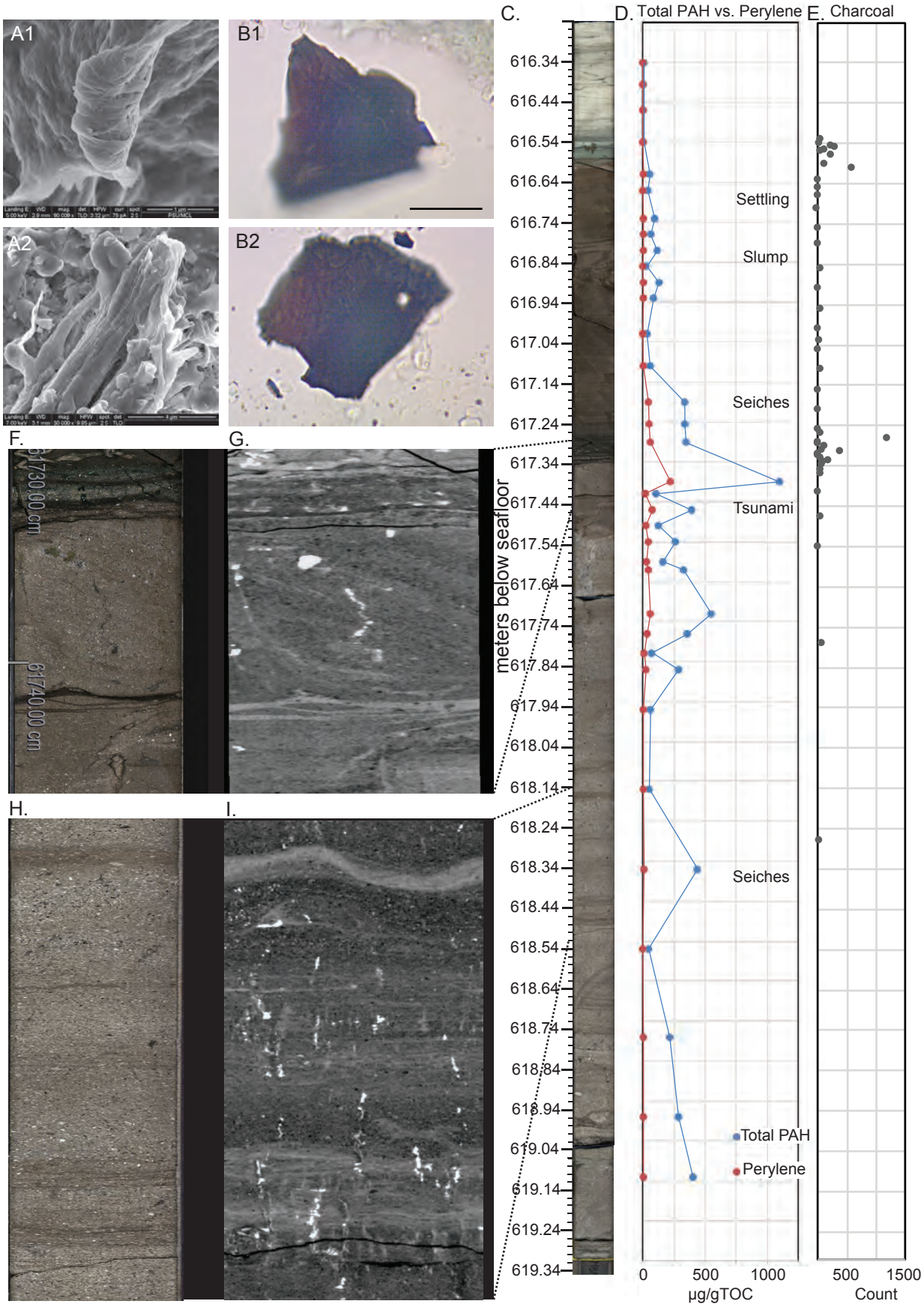
Figure 2. Figure representing key events within first day of the Cenozoic based on numerical modeling, geophysical data, and IODP Expedition 364 drilling. Figure includes two perspectives: a westerly oriented radial profile crossing inner crater rim and shallow shelf and a northeasterly oriented radial profile that crosses opening in crater rim into the Gulf of Mexico. A) Approaching 12 km sized impactor over the pre-impact target of the Yucatán peninsula. B) 100 km wide transient crater and remanent of the impact plume consisting of vaporized/fragmented limestones, evaporites and granitic basement rocks (timescale and geometry based on **5**). C) Collapse of the transient crater with upward-formation of a central uplift starting to undergo dynamic collapse (timescale and geometry based on **5, 9, 44**). D) Morphology after central uplift collapse and peak-ring formation (based on **2, 9**). Initial ocean resurge is depicted entering the crater with timescale based on a dam break model and undergoing melt-water interactions (MWI). E) Ocean resurge completes cresting the peak ring where Site M0077 was drilled. F) Settling of debris within the now flooded crater to form the bulk of the suevite deposit that blankets the peak ring with a zoom in on processes (including seiches) and deposits capping the peak ring. G) Tsunami entering crater from returning rim-wave tsunami and shelf-collapses with a zoom-in of the peak ring K-Pg deposits (timescale based on **34**).

925 Figure 3. Combined analysis of larger clast size portion of the suevite using linescan images
926 of the Hole M0077A split cores; panels A-E show data from visual line logging in orange and
927 machine learning analysis in blue. Panel F shows downhole sonic log from Site M0077 over
928 same interval. Interpreted intervals are shown for molten fuel coolant interaction deposits,
929 resurge of ocean waters cresting peak ring at Site M0077 and start of settling in the now
930 flooded crater to generate the resurge deposit.
931
932 Figure 4. Core 40 from Site M0077 data. A) Scanning electron microscope images of
933 charcoal fragments. B) Reflected light microscope images of charcoal fragments at 1600x
934 magnification. C) Linescan image of Core 40 showing the Transition Layer (Unit 1G) and the
935 uppermost suevite (Unit 2A). D) Total polyaromatic hydrocarbon (PAH) data and the
936 dominant PAH observed in the cross-bedded layer, perylene, both shown as µgrams per
937 gram of total organic carbon (TOC). E) Charcoal counts showing concentrations just above
938 the interpreted tsunami and near the top of Unit 1G. F) Zoom in on linescan image of the
939 crossbedded interval at the top of Unit 2A interpreted as being deposited by a tsunami. G)
940 unwrapped CT scan of same portion of core as F. H) Linescan image of higher energy
941 deposits beneath the tsunami interpreted as seiches. I) unwrapped CT scan of same portion
942 of Core as H.


A.
Distance From Crater Center (km)
50
60
Depth (km)
0.5
1.0
1.5
Suevites
Cenozoic Infill
Shocked
Crystalline
Target
Peak Ring
Annular Trough
Exterior Ring
Inner Ring
Peak
Ring
Annular Tr.
M0077
22°
21°
C1
S1
Y6
Mérida
YAX1
50km
-90
-89
2.0
2.5
3.0
3.5
4.0
4.5
5.0
5.5
6.0
Velocity (km/s)
B.
Core Images
meters below seafloor
615
620
625
630
635
640
645
650
655
660
665
670
675
680
685
690
695
700
705
710
715
720
725
730
735
740
745
750
C.
Units
1E
1G
2A
2B
2C
3A
3B
4
D.
Lithology
Pelagic Carbonate
Transitional Unit
Suevite
Suevite
Resurge Deposit
Suevite & Melt Rock
Breccia
Green & Black
Impact Melt Rock
Black Impact Melt
Rock with clasts
Uplifted Shocked
Target


West
100 km
100 km
Northeast
A.
Asteroid
T=0 min
Water
Sedimentary Rx
Crust
B.
T=1 min
Water
Sedimentary Rx
Impact Plume
Crust
Impact Melt
Mantle
C.
T=3 min
Impact Melt
Sedimentary Rx
Crust
Mantle
D.
T=30 min
Resurge
MWI
MWI
Resurge
Resurge
Breccia
Resurge
Impact Melt
Impact Melt
Crust
Sed. Rx
E.
T=1 hour
Resurge
Resurge
Melt Breccia & Suevite
Impact Melt
Impact Melt
Crust
Sed. Rx
F.
T= Hours
Settling +
Isolated Seiches
Breccia
Melt Breccia & Suevite
Turbid Water
Sed. Rx
Impact Melt
Crust
0 km
-10 km
Settling
Melt breccia
& suevite
Impact melt rock
over shocked
granitoids
G.
T=< 1 day
Tsunami
Sorted Suevite
Semi-Turbid Water
Breccia
Sed. Rx
Impact Melt
Crust
0 km
-10 km
Tsunami
Sorted suevite
Melt breccia
& suevite
Impact melt rock
over shocked
granitoids
10 km
0 km
-10 km
0 km
-10 km
-20 km
-30 km
0 km
-10 km
-20 km
-30 km
0 km
-10 km
-20 km
0 km
-10 km
-20 km


A.
Number of clasts per meter
B.
Clast size
C.
clast
Support
matrix
D.
angular
Roundness
rounded
E.
Size sorting
G.
V_p
Depth (mbsf)
680
690
700
710
Settling
Full Resurge
MFCI w/Initial Seawater
50
100
clasts/m
3
4
-phi
0.5
1.0
A_{matrix}/A_{clast}
0.6
0.5
$4\pi A/P^2$
1
2
σ
3000
3500
V_p (m/s)


A1
B1
A2
B2
C.
D. Total PAH vs. Perylene
E. Charcoal
F.
G.
H.
I.
meters below seafloor
616.34
616.44
616.54
616.64
616.74
616.84
616.94
617.04
617.14
617.24
617.34
617.44
617.54
617.64
617.74
617.84
617.94
618.04
618.14
618.24
618.34
618.44
618.54
618.64
618.74
618.84
618.94
619.04
619.14
619.24
619.34
Settling
Slump
Seiches
Tsunami
Seiches
Total PAH
Perylene
0
500
1000
µg/gTOC
500
1500
Count